

Updates on the Multidimensional Studies of the Proton Fragmentation in the $ep \rightarrow epX$ reaction with CLAS12

Release request of Preliminary Results

Fatiha Benmokhtar¹, Harut Avakian², Timothy B. Hayward³, and Daniel Terrero, Hannah Valenty, Nia Nicholson, Alyssa Gadsby and Aiden Boyer⁴

^{1,4}Department of Physics, Duquesne University, Pittsburgh, PA 15282

²Thomas Jefferson National Accelerator Facility, Newport News, VA 23606

³University of Connecticut, Storrs, CT 06269

1 Abstract

2 Studies of the properties of the azimuthal distributions of hadrons produced in the Target Frag-
3 mentation Region (TFR) serve as a test of our complete understanding of the different mechanisms
4 in the SIDIS production of hadrons and provide additional information on the QCD dynamics that
5 are not accessible with single hadron production in the Current Fragmentation Region (CFR). We
6 present an update of the studies of beam SSA for semi-inclusive protons ($\vec{e}p \rightarrow epX$), produced
7 in the TFR and CFR as well as in a newly identified central region (CR) that can be treated as
8 an interference region between the two previous ones. Preliminary results show that more baryons
9 are produced in the TFR than in the CFR with an asymmetry sign flip between the two, while
10 the asymmetry is consistent with zero in the central region. Some of these preliminary results
11 are requested for release for the 2023 SULI poster session by the undergraduate student Hannah
12 Valenty. Some others are requested to be released for other future conferences.

13 Contents

<small>14</small>	1 Introduction	3
<small>15</small>	1.1 Resources	6
<small>16</small>	1.2 Data Set	6
<small>17</small>	1.3 PID	7
<small>18</small>	1.4 Vertex and Fiducial Cuts	7
<small>19</small>	2 Analysis	8
<small>20</small>	2.1 Distributions	8
<small>21</small>	2.2 Channel Selection	9
<small>22</small>	2.3 Asymmetry Extraction Details	11
<small>23</small>	2.4 Preliminary Results, already released a year ago by the CLAS collaboration	11
<small>24</small>	2.5 Progress in the Analysis	11
<small>25</small>	2.5.1 Defining of the 3 regions	12
<small>26</small>	2.5.2 Integrated Asymmetry Preliminary Results	12
<small>27</small>	2.5.3 X-Feynman Fall 2018 and Spring 2019 comparison	14
<small>28</small>	2.6 Methodology for the Extraction of SSAs	15
<small>29</small>	3 Corrections	17
<small>30</small>	3.1 Proton Energy Loss Corrections	17
<small>31</small>	3.2 Bin Migration Study	20
<small>32</small>	3.3 Q^2 Analysis	22
<small>33</small>	3.3.1 x-Feynman studies versus missing mass	24
<small>34</small>	3.3.2 Eta Analysis	25
<small>35</small>	3.4 Depolarization Factor Study	26
<small>36</small>	4 Results	26
<small>37</small>	4.1 SSAs and Ratio of Fracture Functions Preliminary Results	26
<small>38</small>	4.2 Summary and Future Steps	27
<small>39</small>	4.3 Release Request	29

40 **1 Introduction**

The study of semi inclusive deep-inelastic scattering (SIDIS) process of the electron off a proton target provides access to the three-dimensional spin- and transverse momentum- dependent partonic structure of the nucleon. Hadrons in hard scattering are produced from struck quark in the current fragmentation region (CFR) as well as from target fragments, in the target fragmentation region (TFR). Several kinematic variables used in this analysis include (but are not limited to),

$$Q^2 = -q^2, \quad (1)$$

$$W^2 = (P + q)^2, \quad (2)$$

$$\nu = \frac{q \cdot P}{M} = E - E', \quad (3)$$

$$x = \frac{Q^2}{2P \cdot q} = \frac{Q^2}{2M\nu}, \quad (4)$$

$$y = \frac{P \cdot q}{P \cdot \ell} = \frac{\nu}{E}, \quad (5)$$

$$z = \frac{P \cdot P_h}{P \cdot q} = \frac{E_h}{\nu}, \quad (6)$$

$$\gamma = \frac{2Mx}{Q} = \frac{Q}{\nu}, \quad (7)$$

$$P_h^\perp = P_h \sin \theta_{\gamma h}, \quad (8)$$

$$x_F = \frac{2P_h \cdot q}{|q|W}, \quad (9)$$

$$Y = \frac{1}{2} \log \left[\frac{E_h + p_z}{E_h - p_z} \right], \quad (10)$$

$$\eta = -\ln \sqrt{\frac{x_n^2 M^2 + x_n Q^2}{(1 - x_n) Q^2}} - Y, \quad (11)$$

$$\zeta = E_P/E_t. \quad (12)$$

- 41 ◦ The exchanged virtual photon is defined with its transferred momentum $q = \ell - \ell'$ such that
- 42 ◦ $Q^2 = -q^2$ is the hard scale of the process (the virtuality of the exchanged photon).
- 43 ◦ W is the mass of the hadronic final state, target system.
- 44 ◦ If the electron beam has energy E and the scattered electron has energy E' then ν is defined as
- 45 ◦ the difference between these two quantities.
- 46 ◦ The variables x , y and z are the fraction of target momentum carried by the struck quark, the
- 47 ◦ fraction of beam energy transferred to the virtual photon and the fraction of virtual photon
- 48 ◦ energy carried by the hadron system.
- 49 ◦ The quantity γ describes the relationship between the energy transferred to the struck quark
- 50 ◦ and the virtual photon energy.

51 If $\theta_{\gamma h}$ is the angle between the dihadron momentum and the virtual photon momentum then P_h^\perp
 52 is the projection of P_h perpendicular to the virtual photon direction. The “x-Feynman” variable, x_F ,
 53 is used to differentiate between current and target fragmentation and takes a positive value if the
 54 outgoing hadron moves in the same direction as the incoming electron, in the struck quark center-
 55 of-mass frame. A second variable used for the differentiation between the CFR and TFR is Y , the

56 rapidity in the CM frame, and the η is the rapidity in the Breit frame. A variable especially relevant
 57 for the study of target fragmentation is ζ , the ratio of final state proton energy to initial target energy,
 58 E_t in the γ^* -nucleon center-of-mass frame.

59 The majority of SIDIS studies have focused on the CFR only, in effect leaving half the story
 60 unexplored. Ultimately, the full description of the hadronization process after the hard scattering of
 61 a virtual photon off a quark is needed to describe SIDIS processes. The corresponding theoretical
 62 basis to study the TFR, based on the fracture functions formalism, was established in Ref. [1] for
 63 the integrated over hadron transverse momentum polarization independent part of the cross section.
 64 Recently this approach was generalized [2] to the spin and transverse momentum dependent (STMD)
 65 case.

66 In electroproduction, the polarization state of the virtual photon depends on the longitudinal
 67 polarization of lepton beam, which in turn selects preferentially one polarization state of the struck
 68 quark. The opposite polarization and transverse momentum of a remnant $\bar{q}q$ pair can introduce
 69 correlations between final-state p, n, Λ, \dots hadrons produced in the target fragmentation region and
 70 hadrons produced in the current fragmentation.

71 Assuming a single photon exchange, the SIDIS cross-section for polarized beam and unpolarized targets
 72 can be decomposed into a sum of various azimuthal modulations coupled to corresponding
 73 structure functions. SIDIS cross section has the following form [3, 4, 5]:

$$\frac{d\sigma}{dxdy d\zeta dP_T^2 d\phi_h} = \hat{\sigma}_U \left\{ F_{UU} + \sqrt{2\varepsilon(1+\varepsilon)} F_{UU}^{\cos\phi_h} \cos\phi_h \right. \\ \left. + \varepsilon F_{UU}^{\cos 2\phi_h} \cos 2\phi_h + \lambda_\ell \sqrt{2\varepsilon(1-\varepsilon)} F_{LU}^{\sin\phi_h} \sin\phi_h \right\} \quad (13)$$

74 The unpolarized beam and target contribution $F_{UU} = F_{UU,T} + \varepsilon F_{UU,L}$ is a sum of contributions
 75 from longitudinal ($F_{UU,L}$) and transverse ($F_{UU,T}$) photons.

76 Transverse momentum (P_T) is a kinematic quantity ascribed to the ejected proton post-collision.
 77 In the figure below, the red arrow depicts the direction of the displaced proton, with the solid black
 78 arrow being the vector projection of the proton direction in the hadronic plane, perpendicular to the
 79 photon direction. The variables x, y , and z are, respectively, the fraction of target momentum carried
 80 by the struck quark, the fraction of beam energy transferred to the virtual photon, and the fraction
 81 of virtual photon energy carried by the hadron system. The quantity γ describes the relationship
 82 between the energy transferred to the struck quark and the energy of the virtual photon, $\theta_{\gamma h}$ is the
 83 angle between the hadron momentum and the virtual photon momentum.

84 The depolarization factors in the front of each structure function describe the polarization transfer
 85 from the electron to virtual photon and are dependent on the ratio ϵ of longitudinal and transverse
 86 photon flux [6],

$$\epsilon = \frac{1 - y - \frac{1}{4}\gamma^2 y^2}{1 - y + \frac{1}{2}y^2 + \frac{1}{4}\gamma^2 y^2}, \quad (14)$$

87 with $\gamma = 2m_Nx/Q$ and x, y and Q^2 defined above. The subscripts in the structure functions $F_{UU,LU,\dots}$,
 88 specify the beam (first index) and target (second index) polarization, U, L for the unpolarized and
 89 longitudinally polarized case, respectively.

90 The spin-dependent contributions are obtained from the cross-section equation through the analysis
 91 chain. The modulation of the specific asymmetry is extracted through equation $p_0 + p_1\sin(\phi) +$
 92 $p_2\sin(2\phi)$ for each bin of the variable of focus. The raw asymmetry (A_{LU}) values produced are a useful
 93 form of comparison for trends and dependencies between kinematic variables. The raw asymmetry is
 94 represented by the equation below, where the fractions of positive (N^+) and negative (N^-) helicity
 95 counts prove to be critical.

$$A(\phi)_{LU} = \frac{1}{p} \left(\frac{N^+ - N^-}{N^+ + N^-} \right) \quad (15)$$

96 The ratio of the fracture functions is connected to the raw asymmetry through:

$$\frac{F_{LU}}{F_{UU}} = \frac{A_{LU}}{\sqrt{2\epsilon(1-\epsilon)}} \quad (16)$$

97 The Target Fragmentation Region (TFR) describes the kinematics where the hadrons are produced
 98 from the remnant of the nucleon. The properties of the x-Feynman variable allow this regime to be
 99 identified, as these particles are moving in the backward direction with respect to virtual photon, and
 100 thus assigned a negative x_F value. The converse region to the TFR is the Current Fragmentation
 101 Region (CFR). For the CFR section, hadrons are produced from the ejected quark.

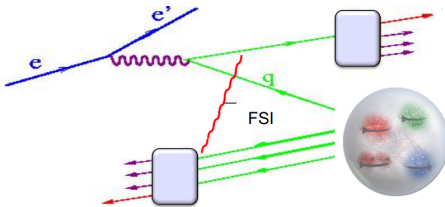


Figure 1: Final State Interactions with TFR on bottom left and CFR in top right.

102 The subscripts in the structure functions $\sigma_{UU,LU}$, specify the beam (first index) and target (second
 103 index) polarization, U, L for unpolarized, and longitudinally polarized case.

104 While in the CFR the structure functions can be presented as convolution of distribution and
 105 fragmentation functions, for the TFR they are presented by so called Fracture Functions (FrFs).

106 Large single beam-spin asymmetries for a longitudinally polarized beam and one or two hadrons
 107 detected in the CFR have been observed at JLab [7], [8], [9], HERMES [10] and elsewhere, which have
 108 been interpreted in terms of higher twist contributions, related to quark-gluon correlations. The data
 109 analyzed here is the largest stats so far for single hadron production in the DIS regime.

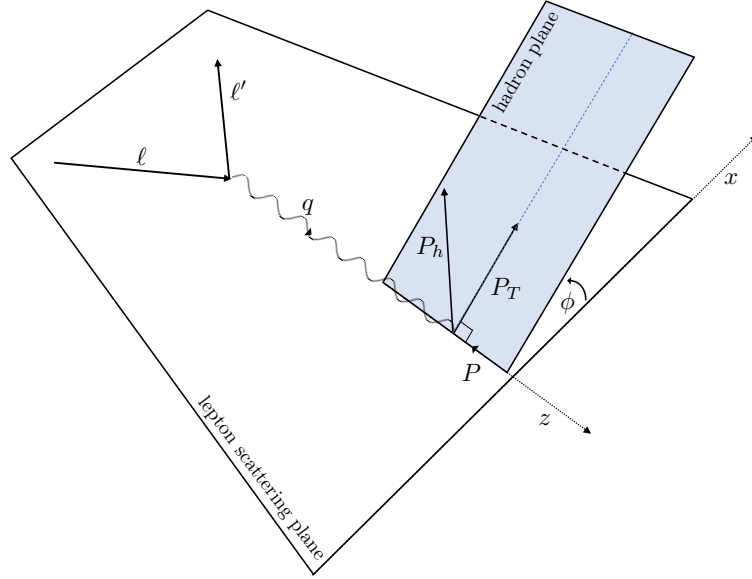


Figure 2: Kinematic plane for TFR hadron production in SIDIS.

110 1.1 Resources

111 The data analysis procedure followed here is close to several fully approved and published RGA first
 112 experiment SIDIS analyses (inclusive π^+ and inclusive $\pi^+\pi^-$ papers) [11, 12]. In addition to these we
 113 make specific use of the following analysis notes

- 114 • RGA Common Analysis: [https://clas12-docdb.jlab.org/DocDB/0009/000949/001/RGA_Analysis_](https://clas12-docdb.jlab.org/DocDB/0009/000949/001/RGA_Analysis_Overview_and_Procedures-08172020.pdf)
 115 [Overview_and_Procedures-08172020.pdf](#)
- 116 • “Back-to-back” (b2b) π^+ -proton analysis: [https://clas12-docdb.jlab.org/DocDB/0009/000935/](https://clas12-docdb.jlab.org/DocDB/0009/000935/007/v3%20to%20be%20submitted%20to%20the%20reviewers.pdf)
 117 [007/v3%20to%20be%20submitted%20to%20the%20reviewers.pdf](#)

118 1.2 Data Set

119 The analyzed data comes from two separate run periods: the RG-A Fall 2018 and Spring 2019 **inbending**
 120 runs with a polarized electron beam incident on unpolarized liquid hydrogen target. This analysis
 121 used **only the forward detector** of CLAS12 which contains a tracking subsystem consisting of drift
 122 chambers in a toroidal magnetic field and high and low threshold Cherenkov counters to identify the
 123 scattered electron and final state hadrons, respectively. The two run periods took data under the
 124 same configurations regarding the CLAS detector components. The only differences between the two
 125 periods was the beam energy, which changed from 10.6 GeV in the fall to 10.2 GeV in the spring. For
 126 the particular run period under consideration was used to calculate any kinematic variables. Beam
 127 polarizations were pretty similar averaging 0.869.

128 The comparison between the two time periods distributions for the two data sets is shown in Fig.
 129 2.1

130 **1.3 PID**

131 The RGA Analysis Overview and Procedures note, pg. 58 [13] goes into significant detail about the
132 common particle identification scheme used for RGA. The first layer of identification is the CLAS12
133 EventBuilder which is used to associate detector responses from various CLAS12 subsystems to par-
134 ticles via an identification protocol. The resulting information is output to dedicated data structures,
135 called HIPO banks, for further physics analysis. This first level of particle assignment by the Event-
136 Builder is relatively loose and significant refinement was added on top of it to improve the PID quality.
137 The identification schema described in the following sections corresponds to the final selection criteria
138 used in this analysis.

139 A full description of the proton (hadron) PID used here with numerous supporting plots can be
140 found in the b2b analysis note starting on pg. 25. The β vs p distribution for hadron candidates can
141 be seen in b2b Fig. 15. The criteria are as follows:

- 142 • Forward Detector
- 143 • > 2 photoelectrons detected in the HTCC (b2b note Fig. 10)
- 144 • > 0.07 GeV energy deposited in the PCAL (b2b note Fig. 11)
- 145 • sector dependent sampling fraction cut (b2b note Fig. 12)
- 146 • “diagonal cut” for electrons above 4.5 GeV (HTCC threshold) (b2b note Fig. 14)
- 147 • $y < 0.75$, not strictly an “electron cut”, but sets the minimum electron energy approximately
148 greater than 2.4 GeV.
- 149 • $|\text{chi2pid}| < 3$

150 Fig. 3 Left shows electron selection using electromagnetic calorimeter, Cherenkov detector and
151 vertex and fiducial cuts. Unlike other single hadron analysis, proton sample from the time of flight
152 versus hadron momentum plot in Fig. 3 Right, proton sample is pretty clean as can be seen in the
153 lower band. Contamination from kaons or pions are negligible (accurate study is underway). For
154 this reason, full proton momentum was considered in this study gaining the largest statistics to-date
155 for single hadron detection with CLAS12.

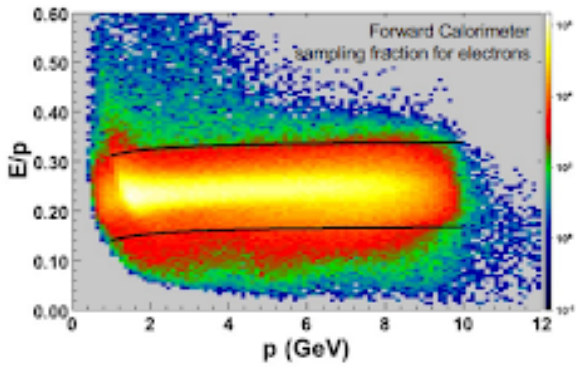
156 **1.4 Vertex and Fiducial Cuts**

157 A detailed discussion and explanation of the fiducial cuts placed on the calorimeter and drift chambers
158 can be found in the RGA Common Analysis note, pg. 70 [13] or on pg. 29 of the b2b note.

159 In this analysis we made sure to remove target wall contributions using appropriate cuts to the
160 electron and proton vertex variables. A sample of fiducial and vertex cuts are shown in the figure 4

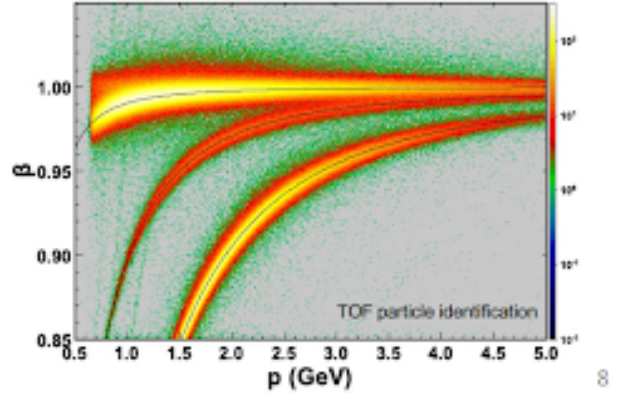
- Electron

- Electromagnetic calorimeter.
- Cherenkov detector.
- Vertex and fiducial cuts.



- Hadron

- β vs p comparison between vertex timing and event start time.
- Vertex and fiducial cuts.



8

Figure 3: Electron identification (left) and hadron identification (right) in CLAS12 forward detector.

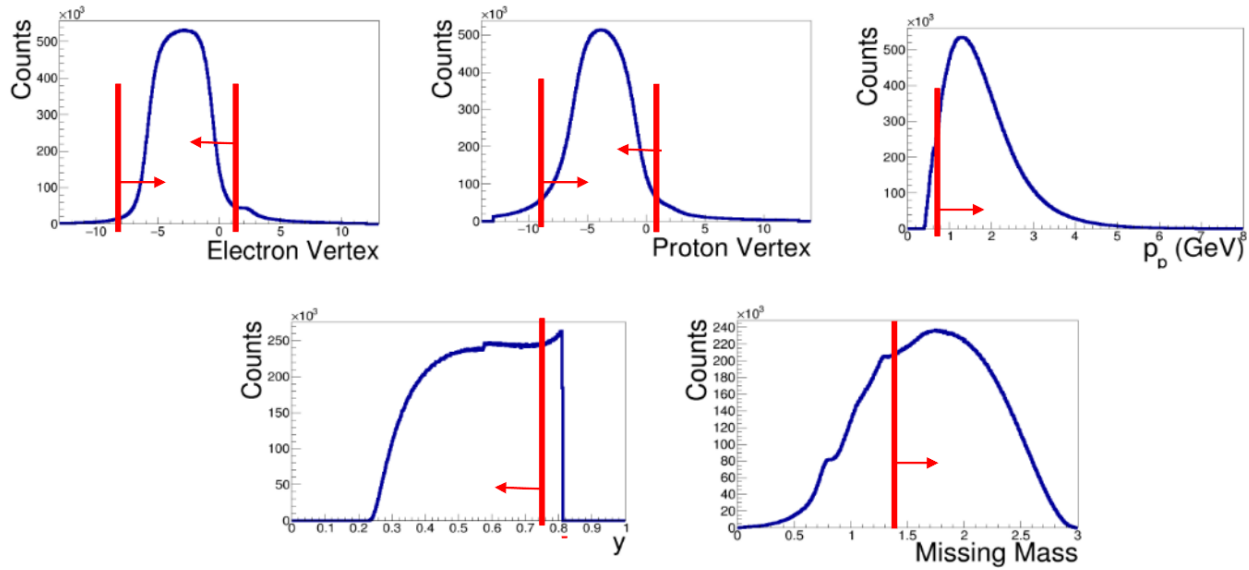


Figure 4: A sample of used cuts.

161 **2 Analysis**

162 **2.1 Distributions**

163 A set of kinematical variables and DIS/SIDIS variables were extracted for fall and Spring Data. Initial
 164 fiducial cuts were applied to some of them reflecting sharp edges as we can see in " y " for example that
 165 is cut at 0.75. The responses for Fall 2018 and Spring 2019 are very similar, except for some deviations
 166 for the variables that are directly related to the beam energy like the momentum of the electron p_e

for example. The number of counts were normalized to be able to stack the two periods on top of each other, as there was more data collected in Spring 2019 than Fall 2018.

Two dimensional plots of some variable combinations are presented as well. This will help gauge the statistics in our asymmetry results later on in the case of low number or non-existing events in some of the covered regions. In particular, the M_x dependence of the other variables is very important, as M_x is key in selecting the clean epX channel as shown in the following section.

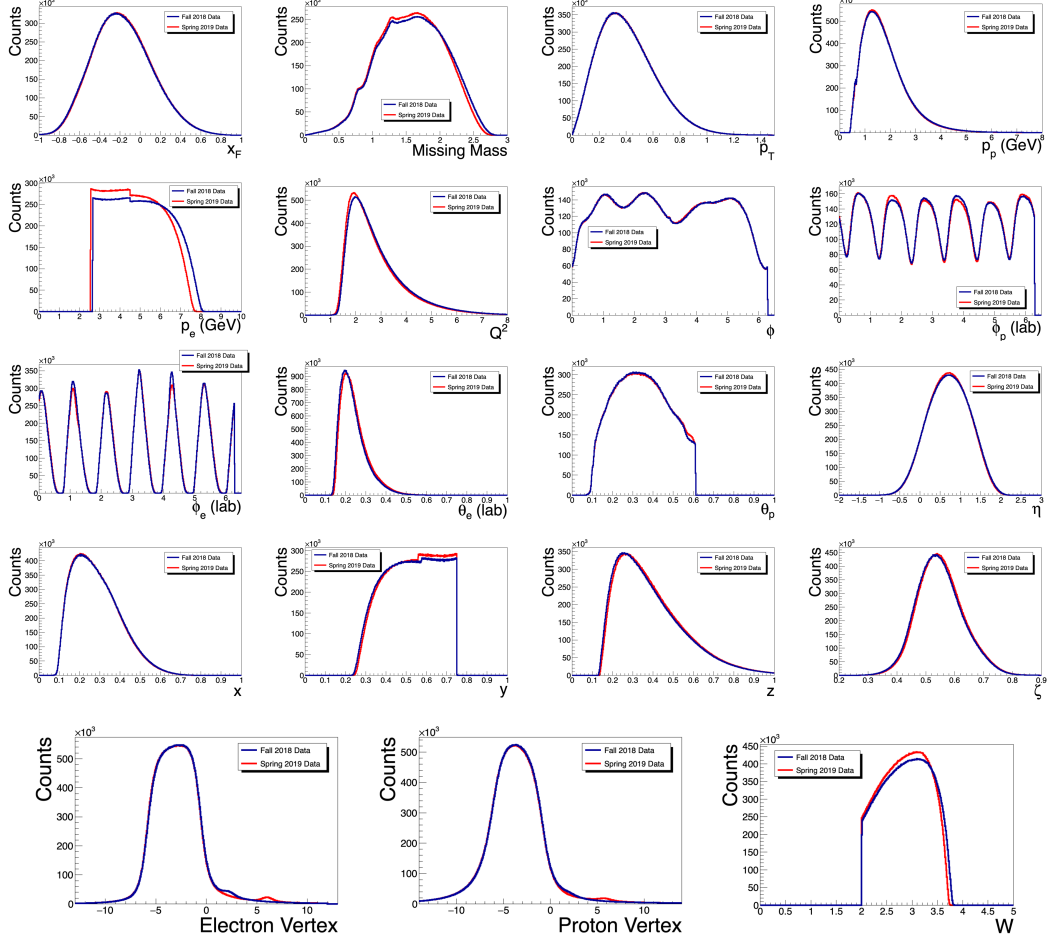


Figure 5: The Fall and Spring data comparisons for all distributions of all relevant variables for the processed data set

2.2 Channel Selection

We are performing an inclusive analysis and would like to avoid contributions from exclusive events. The TMD fracture function formalism does predict any dependence on the missing mass of the system; in FIG. 7 the beam-spin asymmetry is calculated as a function of missing mass in order to investigate the effects that the visible exclusive ρ^0 and f_2 meson events have. Preliminary investigations from CLAS12 and elsewhere indicate that the exclusive ρ^0 asymmetry is sizable (approximately positive 10%) and a noticeable deviation from our linear asymmetry is visible in that region. No change is perceived around the f_2 meson but, due to the wealth of statistics and for safety, a missing mass cut of $M_x > 1.35$ GeV was enforced.

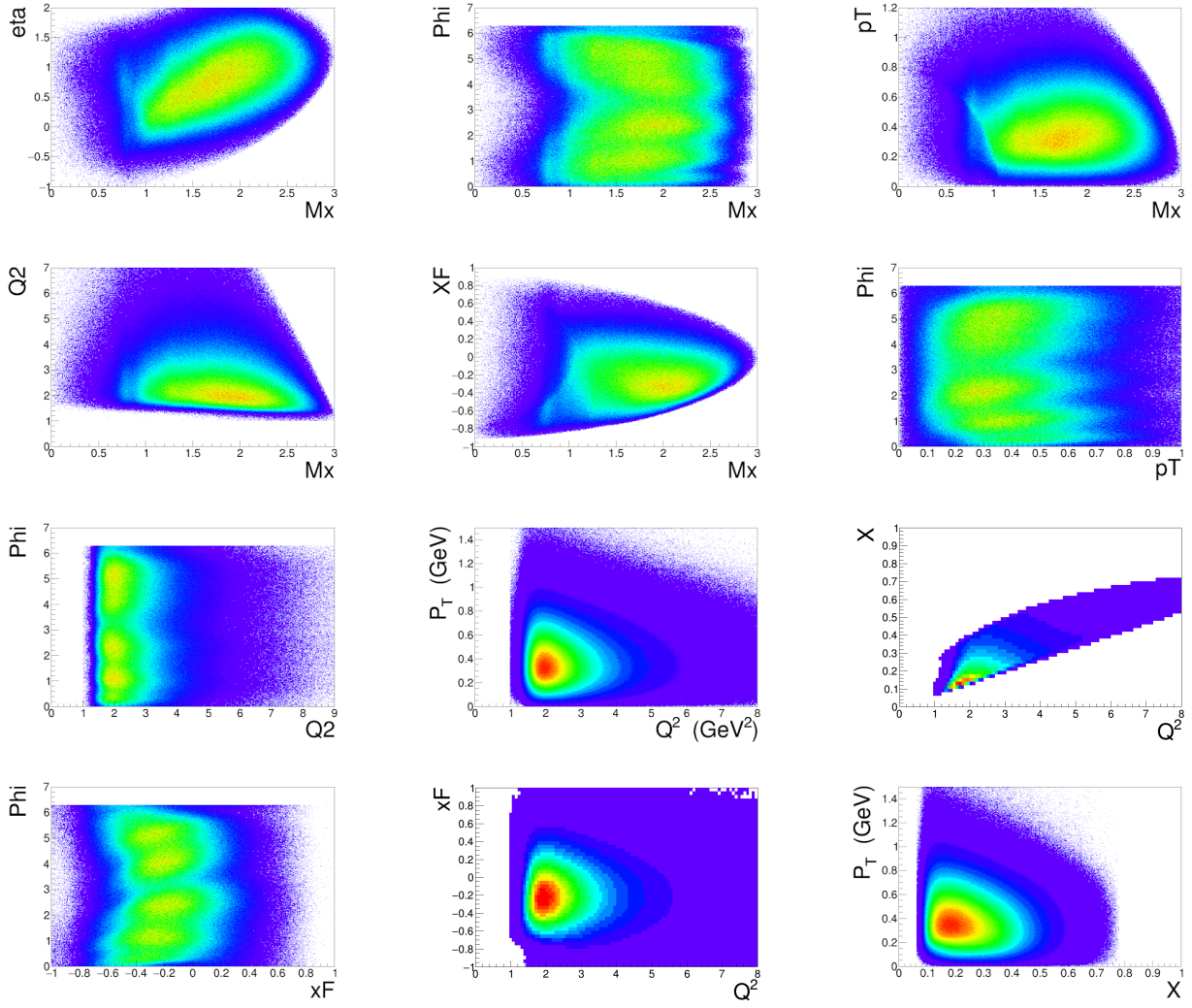


Figure 6: 2 Dimensional distributions of the epX channel

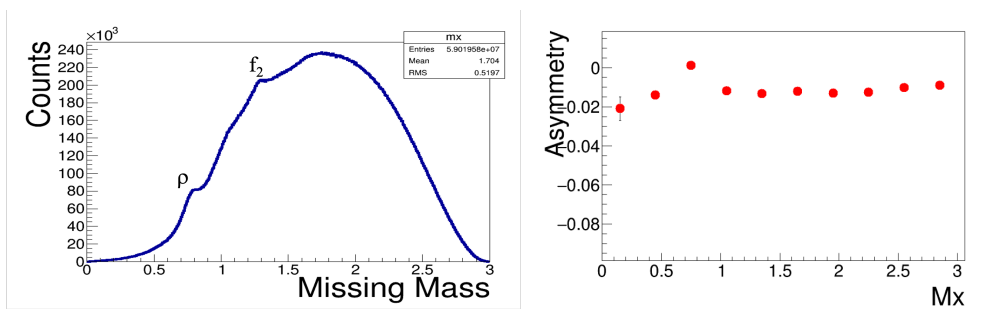


Figure 7: Left: the missing mass of $ep \rightarrow e'pX$. Peaks are visible corresponding to exclusive ρ^0 and f_2 production. Right: the beam-spin asymmetry as a function of the missing mass. Sizable deviations are visible around the ρ^0 mass.

182 **2.3 Asymmetry Extraction Details**

183 To extract the raw single spin asymmetries a four program analysis chain was developed by the
184 Duquesne group. The process begins with designating kinematic variables in a root tree and refining
185 cuts based on which variable is desired for asymmetries. Histograms with bins on ϕ (range of 0 to 6.3
186 (2π) are created for the desired variable, and the counts for positive and negative helicity per bin of
187 the variable of interest (P_T , M_x , x_F , etc...) is output to text files. These helicity text files are passed
188 through a java program which calculates the single spin asymmetry and error values for each bin on
189 ϕ , with the beam polarization (p) equivalent to 0.869.

190 In addition, these asymmetry studies can be refined to any variable of interest by scanning the
191 range of the variable and fitting ($p_0 + p_1 \sin(\phi) + p_2 \sin(2\phi)$) for each bin.

192 These equations are shown below.

$$A(\phi)_{LU} = \frac{1}{p} \left(\frac{N^+ - N^-}{N^+ + N^-} \right) \quad (17)$$

$$\delta A(\phi)_{LU} = \frac{2}{p} \cdot \sqrt{\frac{N^- N^+}{(N^- + N^+)^3}} \quad (18)$$

193 The amplitudes of the fit is what gives us the raw single spin asymmetries.

194 First study was on Missing mass as shown in Fig 7, as the channel selection was very important
195 to avoid leakage from unwanted resonances. Second variable of choice in our analysis chain was x_F ,
196 and detailed study of this variable will be presented later on, given the importance of its results.

197 **2.4 Preliminary Results, already released a year ago by the CLAS collaboration**

198 The beam SSA in semi-inclusive proton electro-production has been studied as a function of some relevant
199 kinematic variables, including the transverse momentum of the proton, P_T (Fig. 9), x-Feynman, x_F
200 (Fig. 8), rapidity, η (Fig. 8). The asymmetry was also extracted as a function of the missing mass of
201 the epX system, to check for any possible contributions from different exclusive processes. The sign
202 flip of the SSA for negative η and positive x_F shows the limits, where the actual current fragmentation
203 starts for forward protons, as they most likely contain the predominantly struck u-quark. Since
204 the beam SSAs in single hadron production, both in target and current fragmentation, are higher
205 twist, the Q^2 -dependence of the asymmetry will provide a crucial test for our understanding of the
206 underlying dynamics. Other variables like ζ and x were also studies in this report.

207 **2.5 Progress in the Analysis**

208 Since the release of preliminary results in 2022, the topic attracted many invited talks given by the
209 analysis team. Since then, a big progress was made in the analysis including analyzing both Fall 2018
210 and Spring 2019 RGA inbending data, combining them and performing multi-Dimensional analysis of
211 the epX channel. In the following, the findings from this updated analysis are presented.

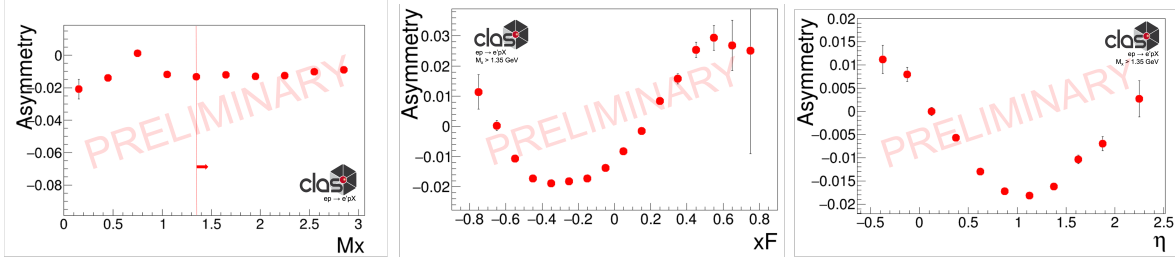


Figure 8: Left: Inclusive proton beam-spin asymmetry as a function of the missing mass of $ep \rightarrow epX$. Center: Inclusive proton beam-spin asymmetry as a function of x_F , . Right: Inclusive proton beam-spin asymmetry as a function of the rapidity in the Breit frame, η .

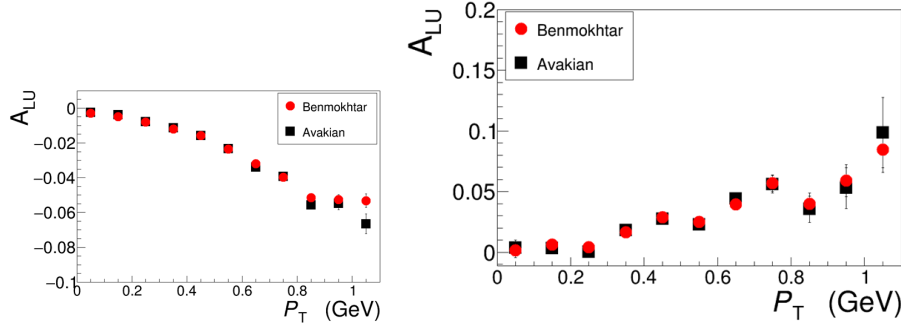


Figure 9: Inclusive proton beam-spin asymmetry as a function of the proton transverse momentum, P_T in the TFR (left) and CFR (right) regions .

2.5.1 Defining of the 3 regions

A more detailed studies of x-Feynman variable were performed, refined binning was used the check get the precise zero intersection. The signature of this zero intersections was confirmed to be close to 0.2. Three physical regions were defined and sketched in 11. These three regions correspond to the Target Fragmentation Region or TFR, Central Region or CR and Current Fragmentation Region (CFR). For the rest of the analysis, we adopted the following limits for each:

- TFR for x_F less than zero
- CR for x_F between zero and 0.3
- CFR for x_F larger than 0.3

2.5.2 Integrated Asymmetry Preliminary Results

Integrated SSA for the three defined SIDIS regions were obtained for Fall 2018, Spring 2019 and the combined data set, that we will be calling Total from now on. The amount of Total data exceeds 150,000,000.00 events.

Fig shows integrated single asymmetries for fall 2018, spring 2019 and for the Total data set. This SSA is presented versus phi.

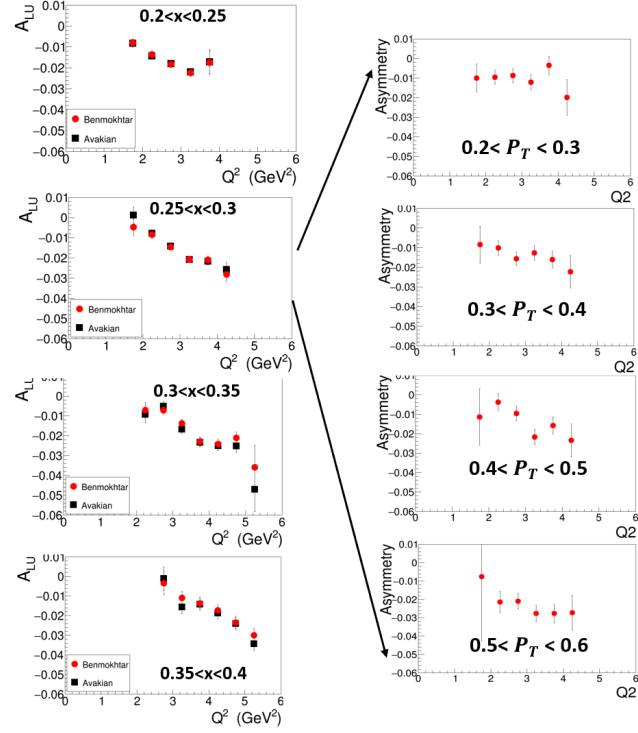


Figure 10: Inclusive proton beam-spin asymmetry as a function of Q^2 in bins of x .

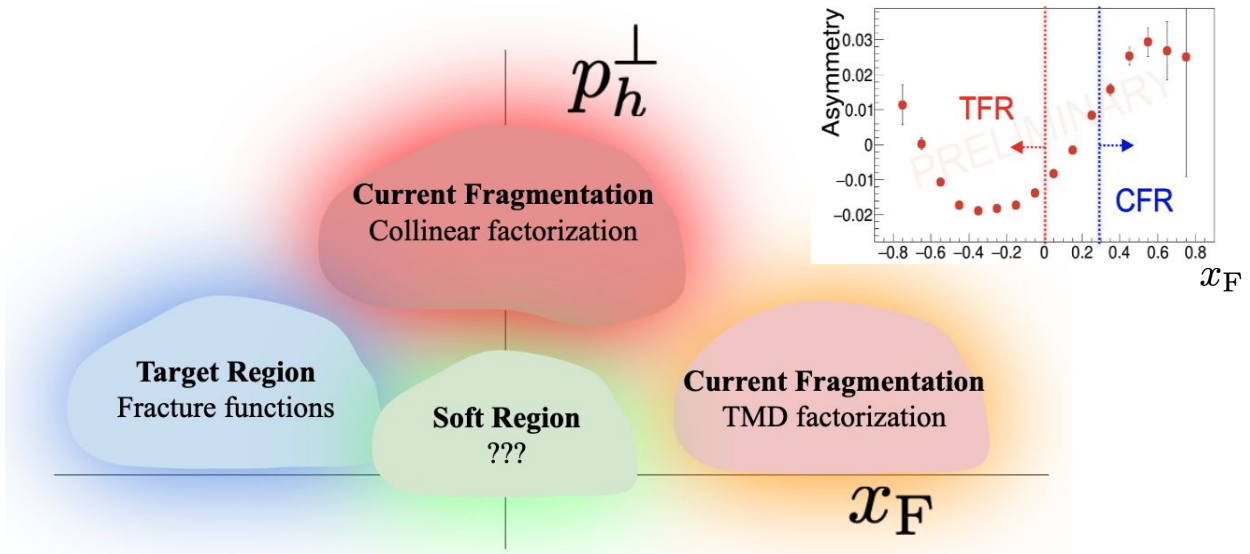


Figure 11: Three SIDIS regions defined from the preliminary data from the 2018 set

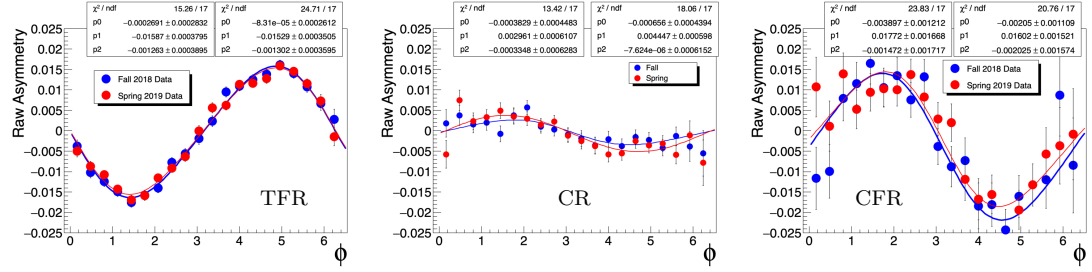


Figure 12: Inclusive proton beam-spin asymmetry integrated over all variables in the TFR region (left) Central region (middle) and CFR region (right) Fall and Spring data comparison.

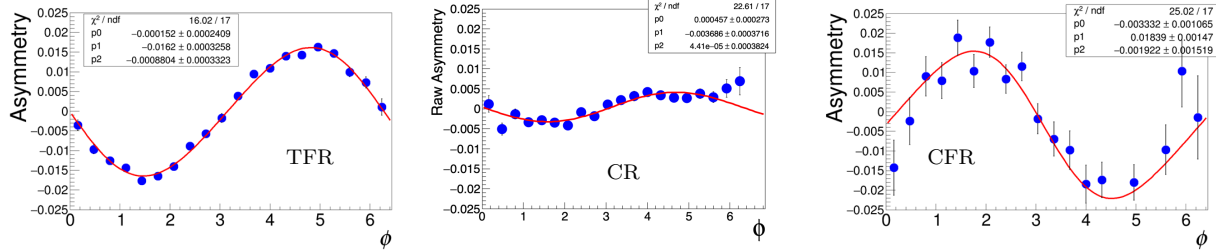


Figure 13: Inclusive proton beam-spin asymmetry integrated over all variables in the TFR region (left) Central region (middle) and CFR region (right) for Total combined data.

227 2.5.3 X-Feynman Fall 2018 and Spring 2019 comparison

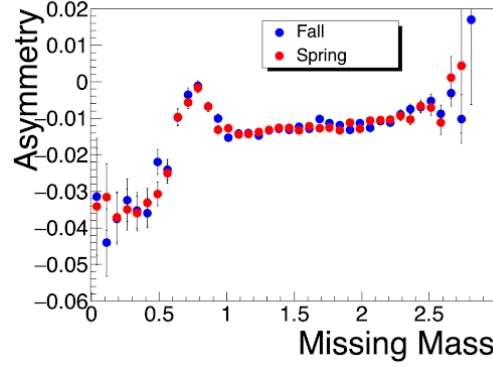


Figure 14: Missing mass SSA comparison for Fall 2018 and Spring 2019

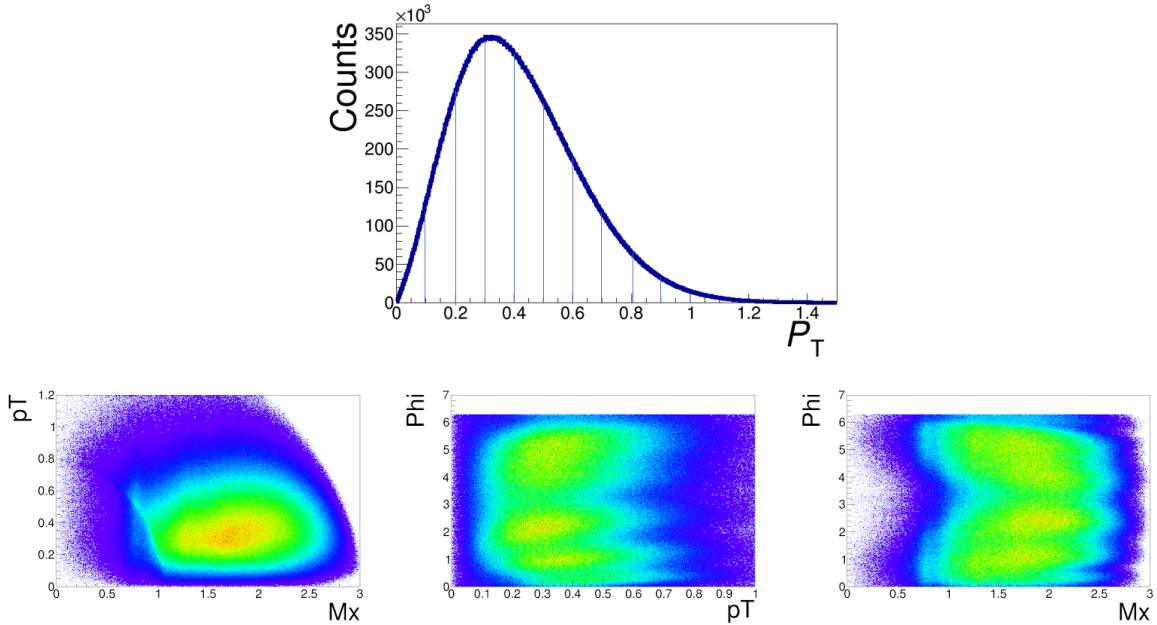


Figure 15: Caption

228 2.6 Methodology for the Extraction of SSAs

229 The CLAS12 detector in Hall B at Jefferson Lab was used for data collection that took place in Fall
 230 2018 and Spring 2019. The analysis of interest is made on the proton DIS from the *epepX* channel.
 231 “*X*” describes the various particles ejected that are not detected. A multi-dimensional approach was
 232 implemented to gain many perspectives on the data. Raw data was treated using a java analyzer,
 233 where initial fiducial cuts were applied and a text file with data events for different physics DIS/SIDIS
 234 and kinematic variables was created.

235 In previous iterations of this study, the Fall 2018 and Spring 2019 text files were kept separate to
 236 do individual analysis and then comparison of their results. However, the study evolved where the
 237 two original files were combined for a Total data text. This increased the events greatly with over
 238 150 million in all. The file was passed through our root analyzer, where the variables were stored in a
 239 root Tree for future use. Asymmetry calculations were performed on most of the physics variables and
 240 trend dependencies were studied. Finally, depolarization corrections were applied to the asymmetry
 241 to get the ratio of fracture functions.

242 To illustrate the analysis steps, the example of the asymmetry extraction for the Transverse Mo-
 243 mentum P_T in the TFR region will be detailed.

244 First, the transverse momentum P_T graph is sliced into equal bins of size 0.1 as shown in Fig. 15
 245 Upper plot. P_T dependence versus Trento ϕ and Mx is looked, as well as Mx dependence on ϕ . A
 246 cut on Mx 1.35 is applied.

247 The number of counts per helicity state for 20 bins in ϕ for each slice on P_T were then extracted and
 248 used to calculate the raw asymmetry. Fig. 16 represent the results of these asymmetry distribution
 249 versus ϕ for different bins on P_T .

250 Next, the modulation of the asymmetry for each bin of P_T is fitted versus ϕ with the equation
 251 $p_0 + p_1 \sin(\phi) + p_2 \sin(2\phi)$. The amplitude p_1 and its associated statistical error is extracted. Finally,

²⁵² p_1 is divided by the beam polarization and the result is the single spin asymmetry associated to the
²⁵³ mean of each bin on P_T .

²⁵⁴ Finally, the result of this part of the analysis is shown in Figure 17.

²⁵⁵ This study will be followed by the depolarization normalization which allows the extraction of the
²⁵⁶ ratio of the fracture functions.

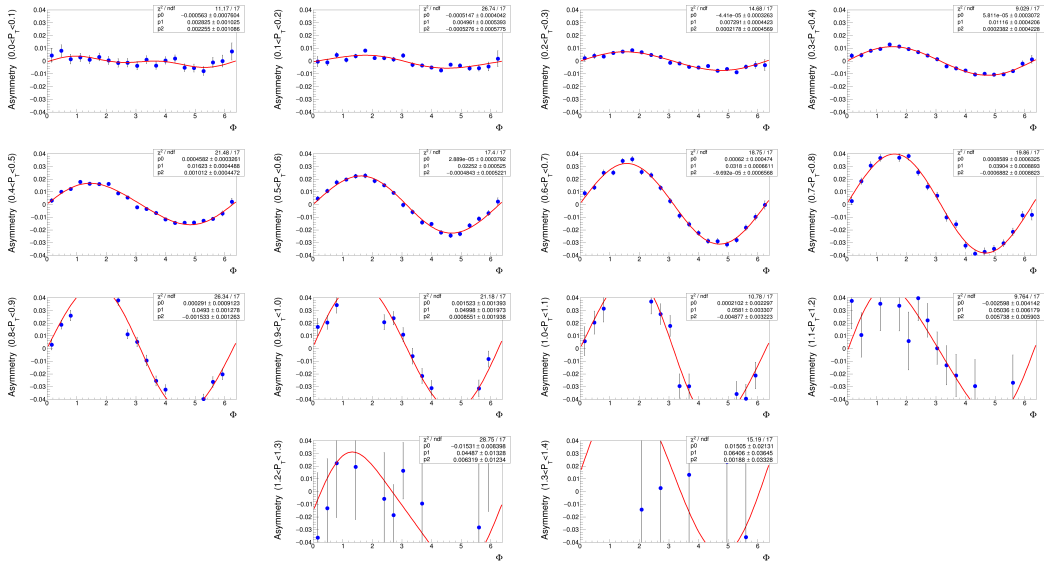


Figure 16: $\sin(\phi)$ Modulation versus Transverse Momentum.

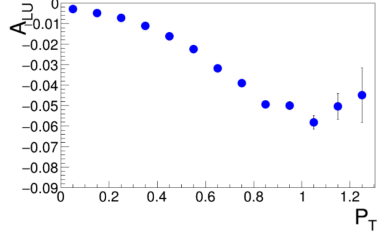


Figure 17: Single Spin Asymmetries for the Transverse Momentum P_T in the TFR region.

257 3 Corrections

258 3.1 Proton Energy Loss Corrections

259 Momentum corrections analysis have been described in great detail in the exclusive π^0 electro-
 260 production analysis note of Andrey Kim [14], https://clas12-docdb.jlab.org/DocDB/0009/000948/001/AKim_pi0_note.pdf, starting on page 41. for the epX channel we took formula for the correction
 261 derived by Andrey Kim and corrected our data. In short, and our understanding from the document
 262 is: the most significant contribution for proton momentum corrections comes from the energy loss
 263 effect when a proton loses its energy via passing through the passive materials between the vertex and
 264 the tracking detectors (DC). The GEMC simulation of the detectors including the passive material
 265 of CLAS12 was used to propagate and develop the proton energy loss correction as a function of its
 266 momentum and angle. The energy loss corrections are developed separately for two regions: $\theta < 27^\circ$
 267 and $\theta > 27^\circ$. As higher angle protons are propagated through more material in the central detectors,
 268 such as CVT or HTCC.

270 The technique consists of the study of the difference between generated and reconstructed events
 271 and correct for any deviations that will be associated to Energy loss:

$$\Delta P = P_{gen} - P_{rec} \quad (19)$$

272 The momentum distribution is sliced and for each momentum slice the ΔP distribution. The
 273 mean values from the contributions are plotted as a function of momentum, and fit using exponential
 274 function:

$$\Delta P = e^{p_0 + p_1 P} + p_2 \quad (20)$$

275 Energy loss correction formula was implemented in the analyzer by T. Hayward and in this report
 276 we made use of it to study its effect to our epX channel.

277 Two dimensional study of the momentum P versus ΔP was performed and we can see the difference
 278 in these plots for integrated coverage then the two angle regions, separately in Figs. 18 19 20. One
 279 dimensional plot of ΔP for the three sets are presented in Fig. /ref1Ddeltap

280 Figs. 22 and 23 represent the sliced bin distributions for the two sets of angles, respectively.

281 Energy Loss corrections were applied to all the variable and the effect on x-Feynmann is presented
 282 in the Fig. 26.

283 For the rest of the note, all the studies, extracted SSA and Fracture Functions ratios are extracted
 284 with energy loss corrections.

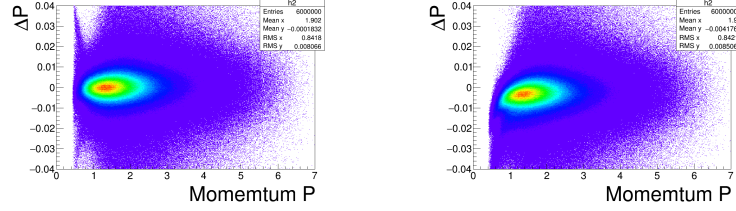


Figure 18: Distribution without (left) and with (right) Energy loss corrections energy loss correction

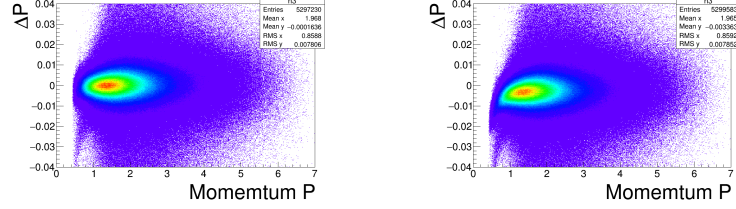


Figure 19: Distributions without (left) and with (right) energy loss corrections for proton angles less than 27 deg

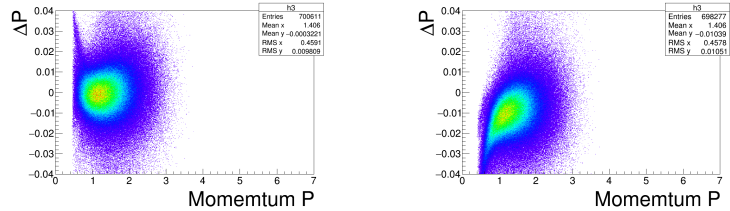


Figure 20: Distributions without (left) and with (right) energy loss corrections for proton angles larger than 27 deg

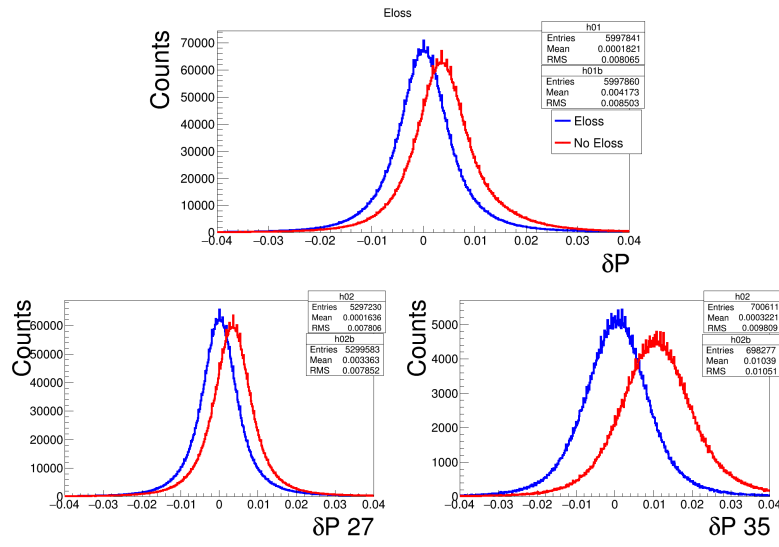


Figure 21: Upper plot: δP with Eloss (blue) vs no Eloss (red). Lower plots: δP divided into two angle ranges 0 to 27 then 27 to 35 deg for forward detection.

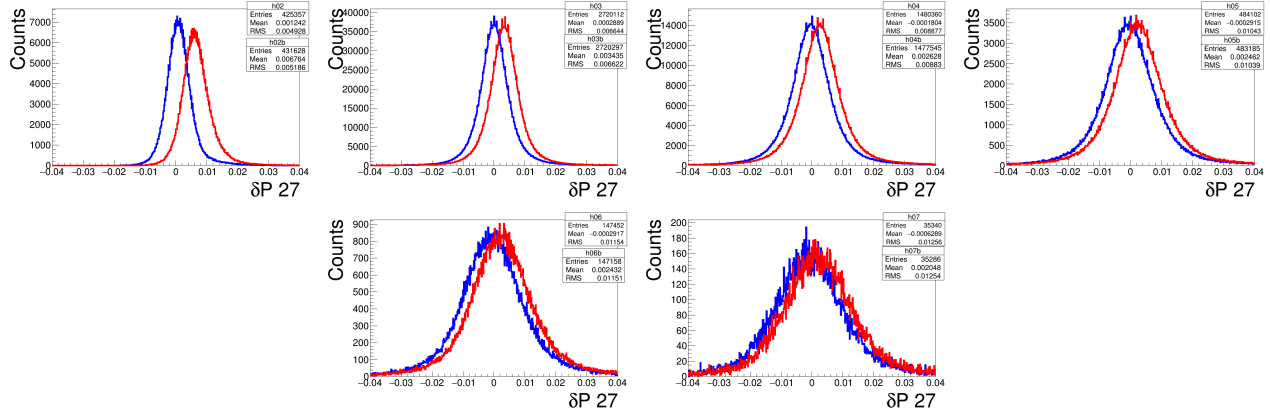


Figure 22: δP with and without energy loss sliced on proton momentum bins for angles less than 27 deg.

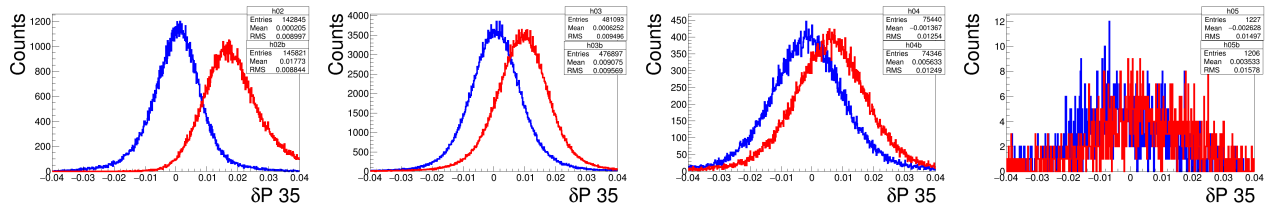


Figure 23: Proton momentum with and without Eloss corrections, for angle between 17 and 35 deg

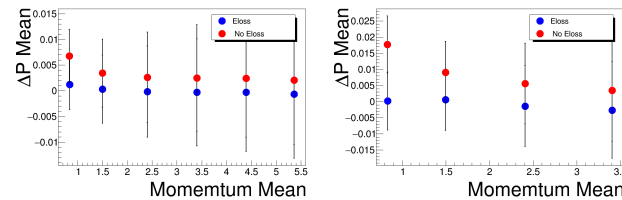


Figure 24: δP versus average momentum bins for Left: up 27 deg, Right: from 27 to 35 deg

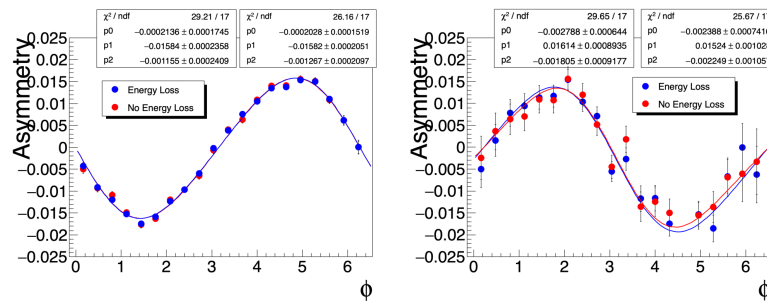


Figure 25: Integrated Total Single Spring Asymmetry comparison with and without Energy Loss corrections

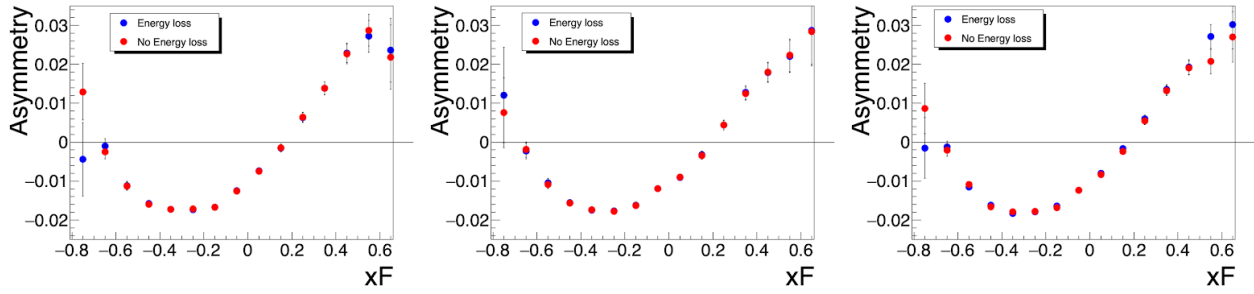


Figure 26: Effect on Energy loss corrections on x-Feymann for Fall 2018(Upper left), Spring 2019 (Upper right) and Total data sets

285 3.2 Bin Migration Study

286 When working with histograms modeling high numbers of events, it is possible to encounter event
 287 migration across bins. This phenomena is due to the finite resolution of the kinematic variables
 288 used to analyze the single-spin asymmetries. The contributing error from migration effects can be
 289 minimized if the difference of calculated asymmetry in neighboring bins is insignificant [hayward].

290 To test if significant migration occurred in the single-spin asymmetry study, Monte Carlo simulated
 291 data was employed. This text file mirrored the existing experimental tree and variable branches format,
 292 with the addition of generated values. Each kinematic variable had a corresponding Generated and
 293 Reconstructed value, where in terms of the experiment, generated values are simulated prior to hitting
 294 the detector and reconstructed are produced from after passing through the detector. The capability
 295 to compare events prior to and following detection provides the tools needed for determining if the
 296 error is significant.

$$\Delta(\text{variable}) = \text{Reconstructed} - \text{Generated} \quad (21)$$

297 A complete picture of the possible migration for each variable was produced by two one-dimensional
 298 histograms and a error dot plot. The first histogram outlined the delta test, where delta is equivalent to
 299 reconstructed subtracted by generated. If the peak of the histogram was close to zero it suggested in-
 300 significant error. A comparison between generated and reconstructed composed the second histogram,
 301 with one-dimensional plots of the same variable in the generated and reconstructed forms drawn in
 302 the same canvas. This aided in double checking the event counts simultaneously present in the text
 303 file. Finally, the error dot plot was a production of the ratio of the mean generated data over the mean
 304 reconstructed data. If the plot displayed a line of points around one, the lack of deviation from that
 305 value would indicate a strong case for insignificant migration error. To produce the error bars for this
 306 plot, a propagation technique was used to statistically combine the error from unique generated and
 307 reconstructed data sets. Below is the propagated error equation used in the ratio calculation program.

$$\text{Prop.Error} = \frac{\langle \text{Gen.} \rangle}{\langle \text{Recon.} \rangle} \cdot \sqrt{\left(\frac{\sigma_G}{\sqrt{N_G} \cdot \langle \text{Gen.} \rangle} \right)^2 + \left(\frac{\sigma_R}{\sqrt{N_R} \cdot \langle \text{Recon.} \rangle} \right)^2} \quad (22)$$

308 Below are the three variables (P_T , x_F , and Q^2) pre-bin migration analysis for determining the
 309 necessity of additional bin corrections.

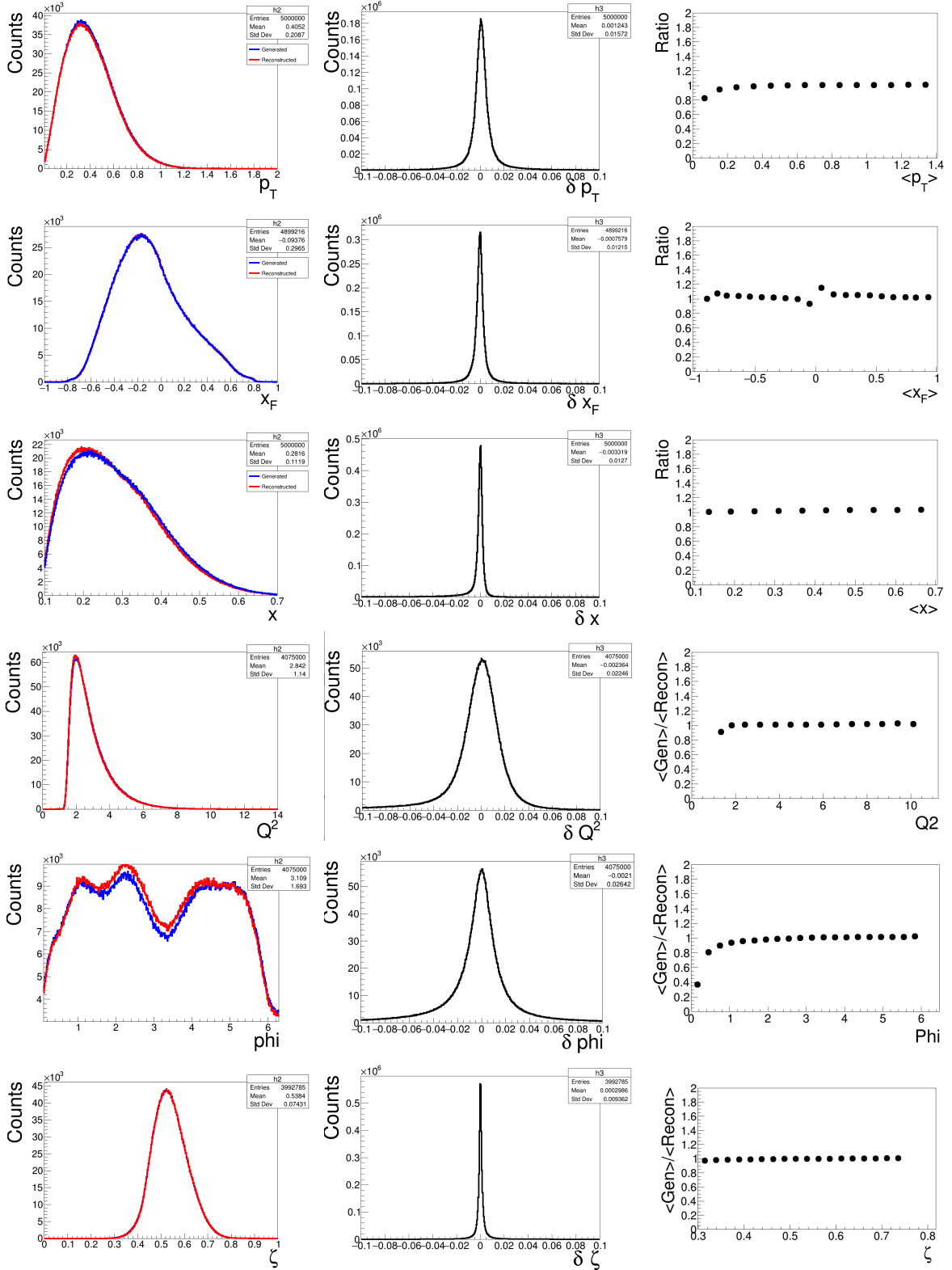


Figure 27: Bin Migration study for different variables.

310 3.3 Q^2 Analysis

311

313

319

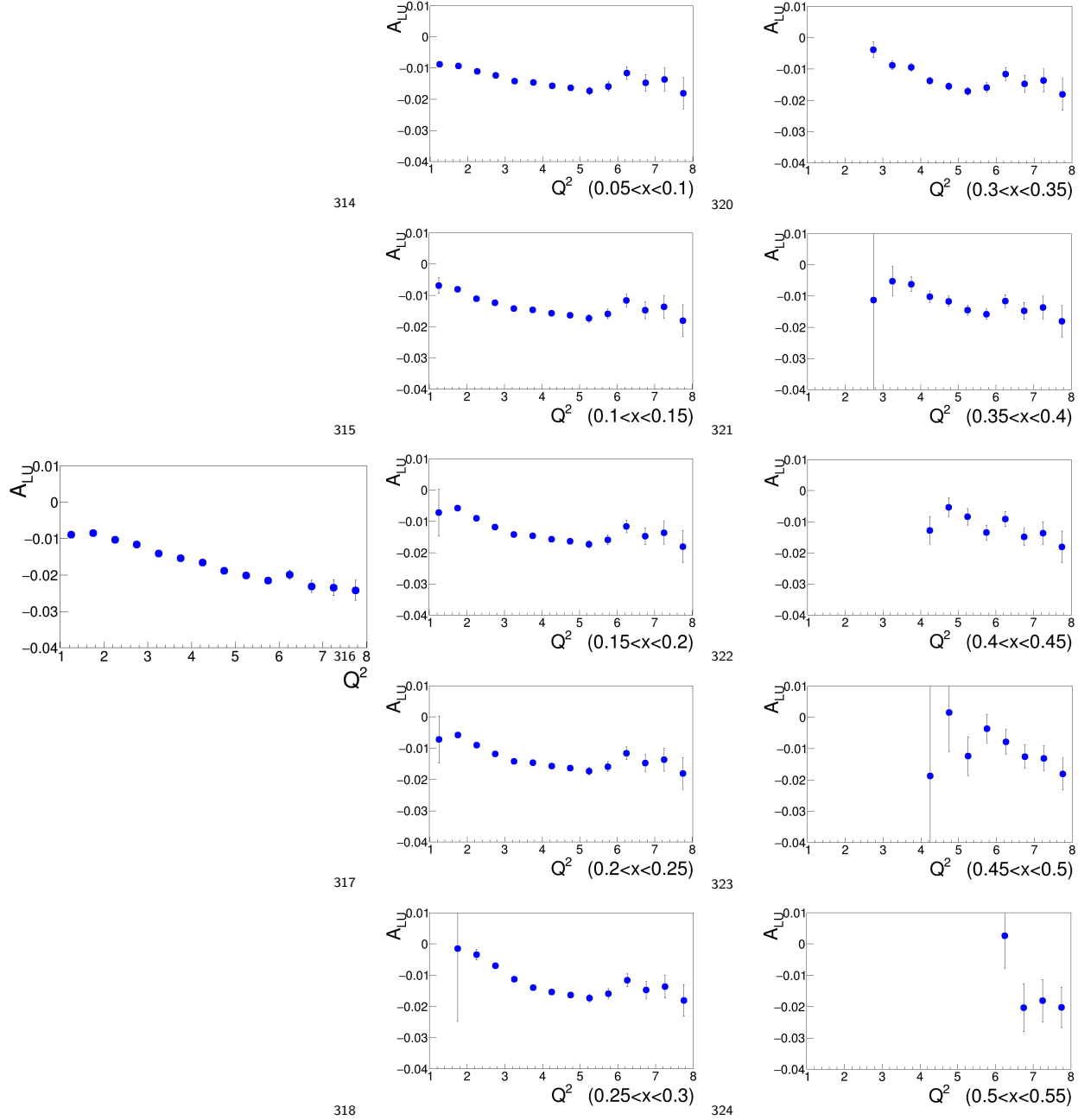


Figure 28: Left: Q^2 without any cut on x , Right: Q^2 with cuts between $0.05 < x < 0.55$

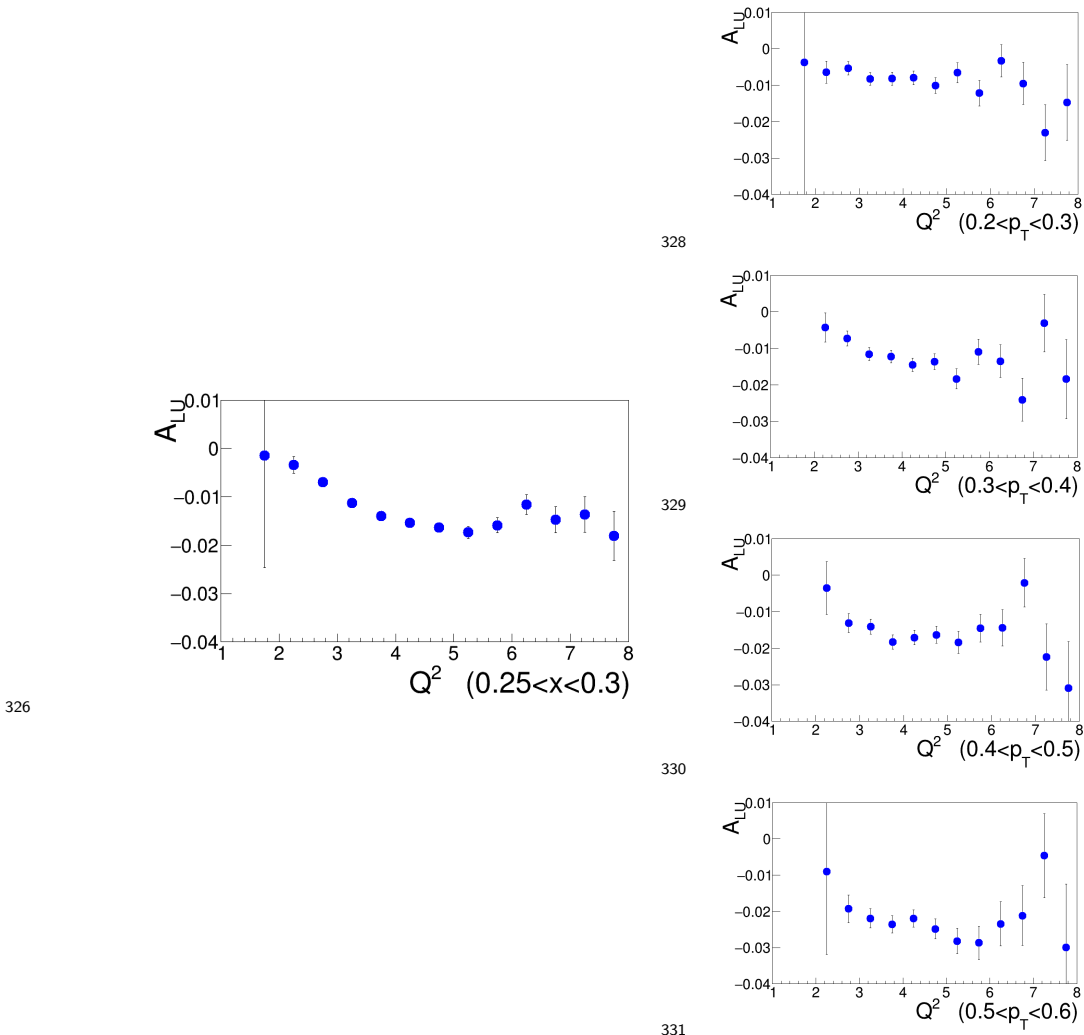


Figure 29: Left: Q^2 with cut $0.25 < x < 0.3$ without any cut on pT , Right: Q^2 with cuts between $0.2 < pT < 0.6$

332 We have performed the study of x-Feynman versus missing mass, by scanning the missing mass
 333 and check for any leakage of the resonances to the $e p X$ channel.

334 **3.3.1 x-Feynman studies versus missing mass**

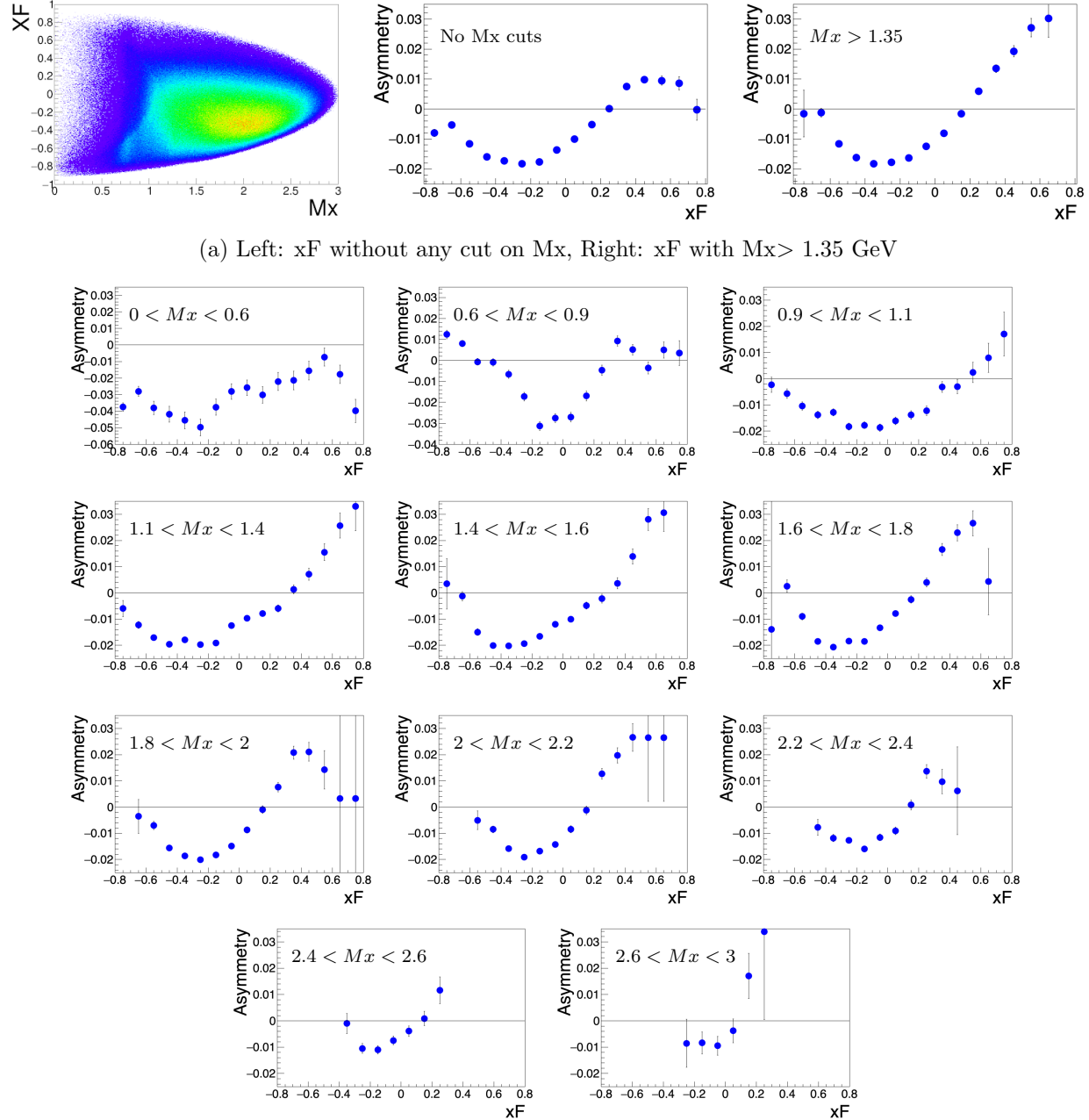


Figure 30: Asymmetry vs x-Feynman with energy loss and binning in missing mass for Total combined data.

335 **3.3.2 Eta Analysis**

336

338

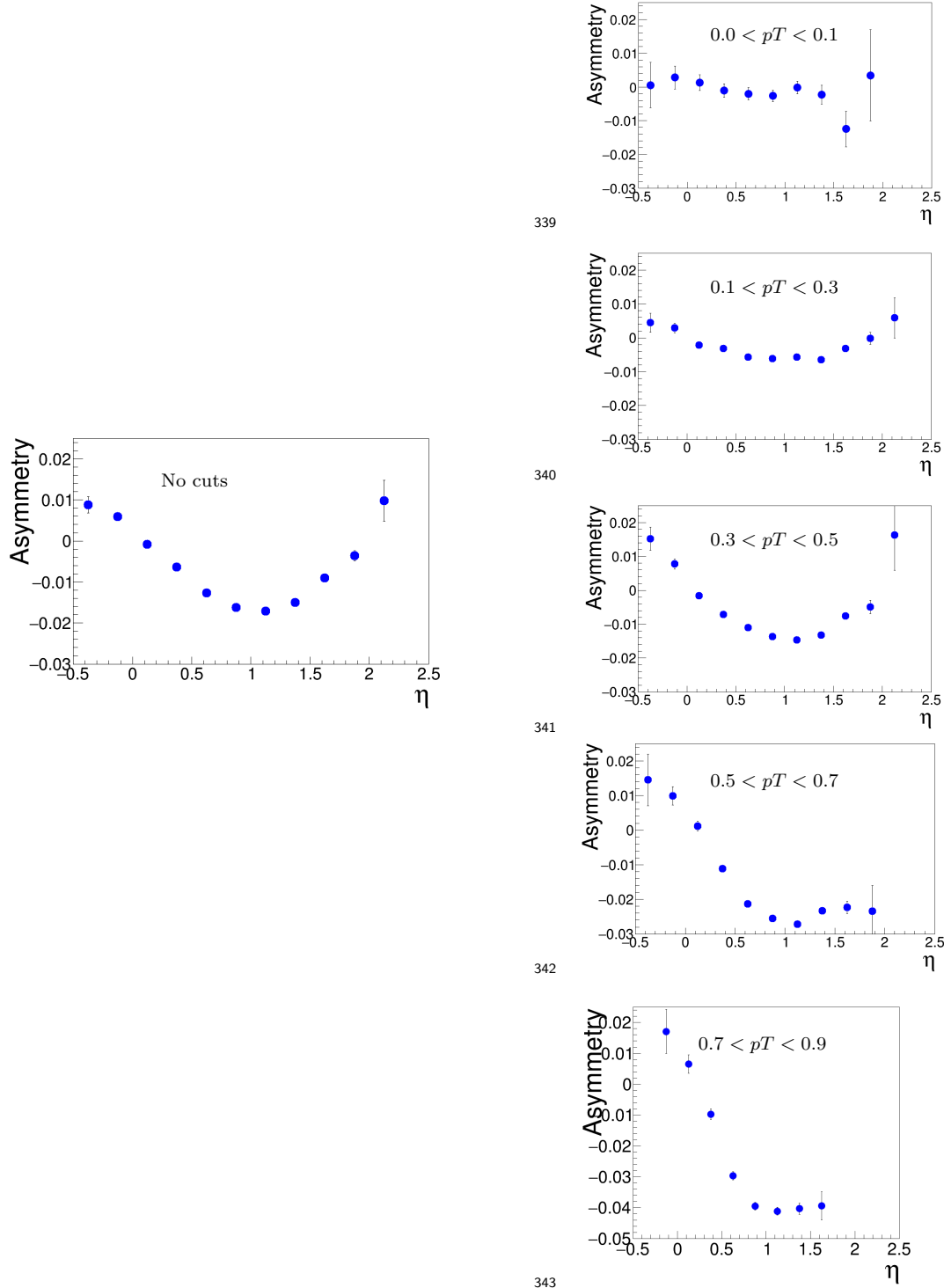


Figure 31: Left: Eta with no cuts, Right: Eta with cuts between $0.0 < pT < 0.9$

344 **3.4 Depolarization Factor Study**

345 To normalize the raw asymmetry and convert them to values of the fracture function ratio ($\frac{F_{LU}}{F_{UU}}$)
 346 values, a depolarization factor is necessary. This factor is mathematically represented by the function
 347 $\sqrt{2\epsilon(1-\epsilon)}$. The value of the depolarization factor was calculated for each bin of a focus variable and
 348 was simply incorporated into the measurement of the fracture function ratio by dividing the amplitude
 349 (A_{LU}) of the raw asymmetry ($A(\phi)_{LU}$) by the kinematic factor. Depolarization factors for Q^2 , x_F P_T
 350 in the TFR and P_T in the CFR are presented in Fig. 32. The values of the depolarization factors fall
 351 around 0.6 to 0.7 and the variable with most stability is P_T in the TFR region.

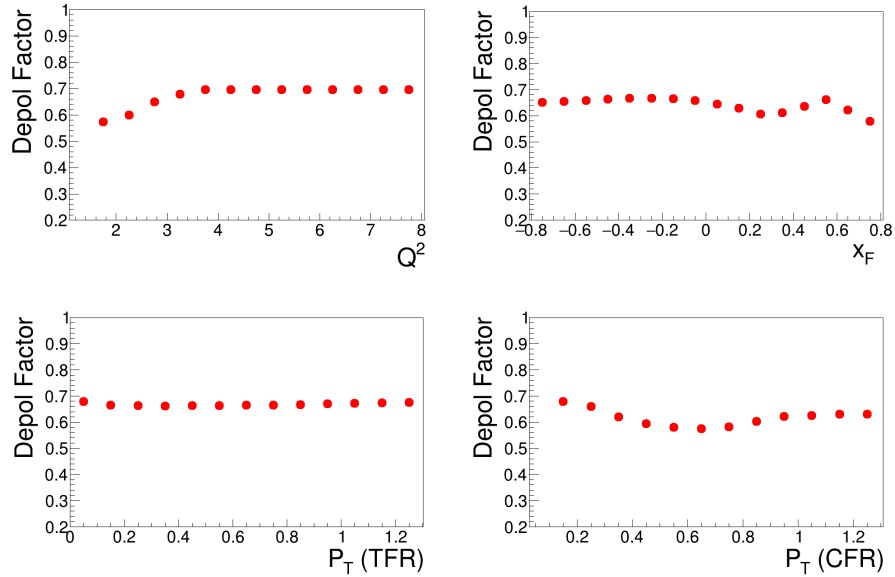


Figure 32: Depolarization factor for different variables

352 **4 Results**

353 **4.1 SSAs and Ratio of Fracture Functions Preliminary Results**

354 Both raw asymmetries and fracture functions were calculated and plotted for several kinematic vari-
 355 ables. The following figures give the results for the combined A_{LU} and $\frac{F_{LU}}{F_{UU}}$ trends for different
 356 kinematical variables. All the results have fiducial cuts, target cut, $Mx > 1.35$ cut and energy loss
 357 corrections applied.

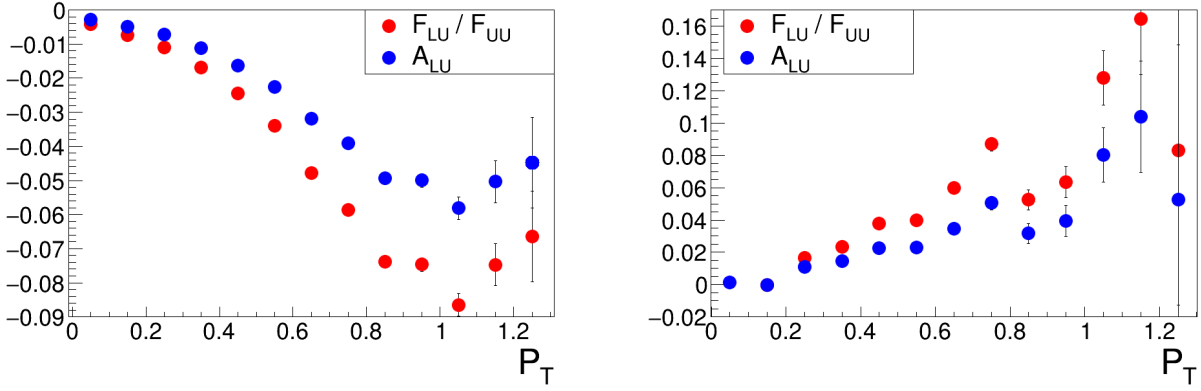


Figure 33: Raw and Normalized SSAs for p_T (GeV) for TFR and CFR [PRELIMINARY].

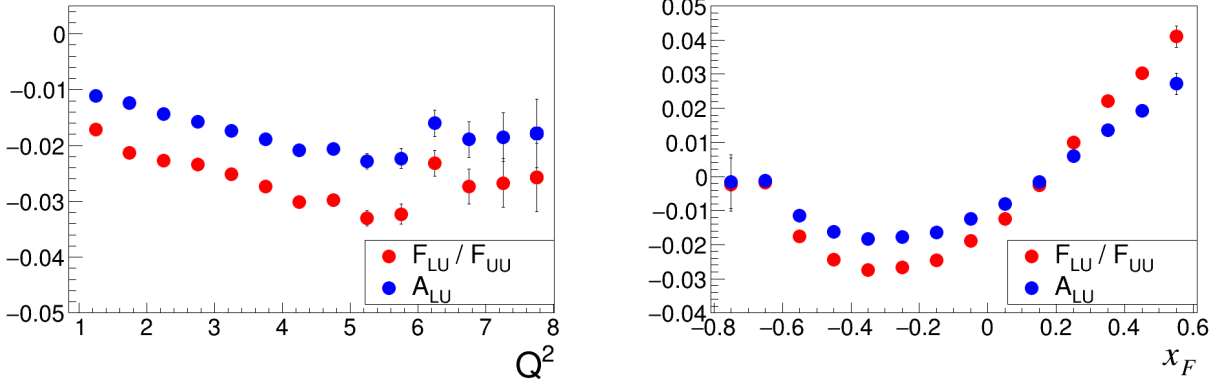


Figure 34: SSAs for x_F and Q^2 (GeV) Kinematic Variables [PRELIMINARY].

358 4.2 Summary and Future Steps

359 In this document we presented preliminary results of the multi-dimensional analysis for the $e p X$
 360 DIS channel. Many variables have been looked at. Fiducial and vertex cut in addition to channel
 361 selection cuts were applied. Detailed Energy loss corrections were applied. Our study showed that bin
 362 migration are so small and there is no need to applying the correction. Finally, depolarization studies
 363 were performed to normalize raw asymmetry to the ration of fracture functions.
 364 Future work will consist on continuing with the systematical corrections and specifically check the
 365 effect of small fluctuation on variables like Q^2 in the resulting asymmetries.
 366 We plan to write a detailed and final analysis note in the next few months with final results for a
 367 review by the collaboration.

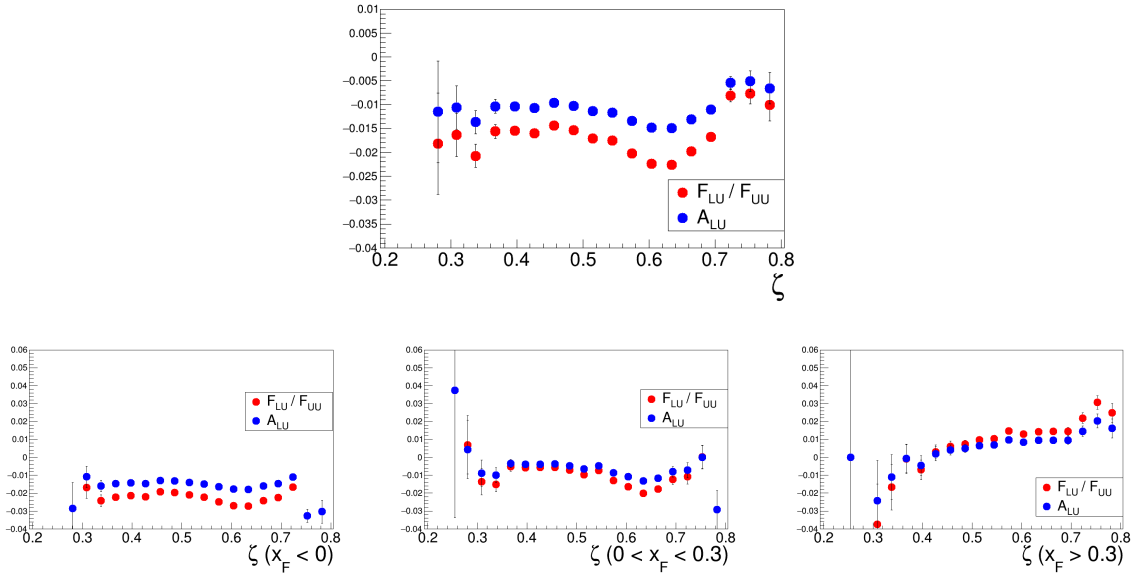


Figure 35: Asymmetry and Fracture Function ratio Graph for ζ . Top: Total. Bottom: from left to right: TFR, CR and CFT defined by the x_F selected regions

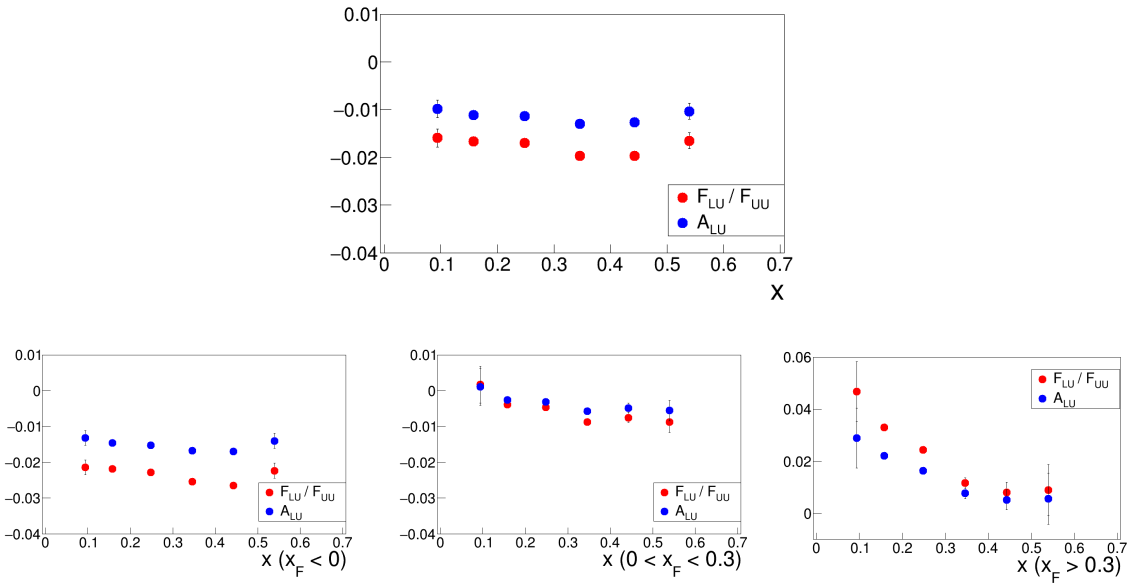


Figure 36: Asymmetry and Fracture Function ratio for x . Top: Total. Bottom from left to right: TFR, CR and CFR defined by the x_F selected regions

368 **4.3 Release Request**

369 We request to release the following plots for Hannah Valenty to present a poster at the Jefferson SULI
 370 2023 session. These plots are x-Feynman with energy loss corrections for the Total data, and the
 371 transverse momentum plot in TFR and CFR regions.

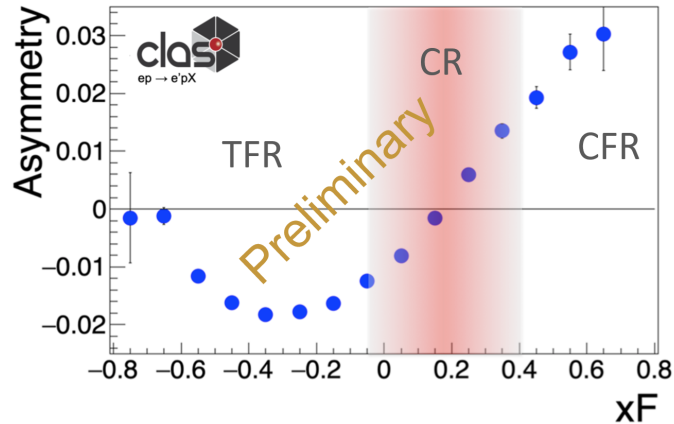


Figure 37: SSAs for x-Feynman defining TFR, CR and CFR regions.

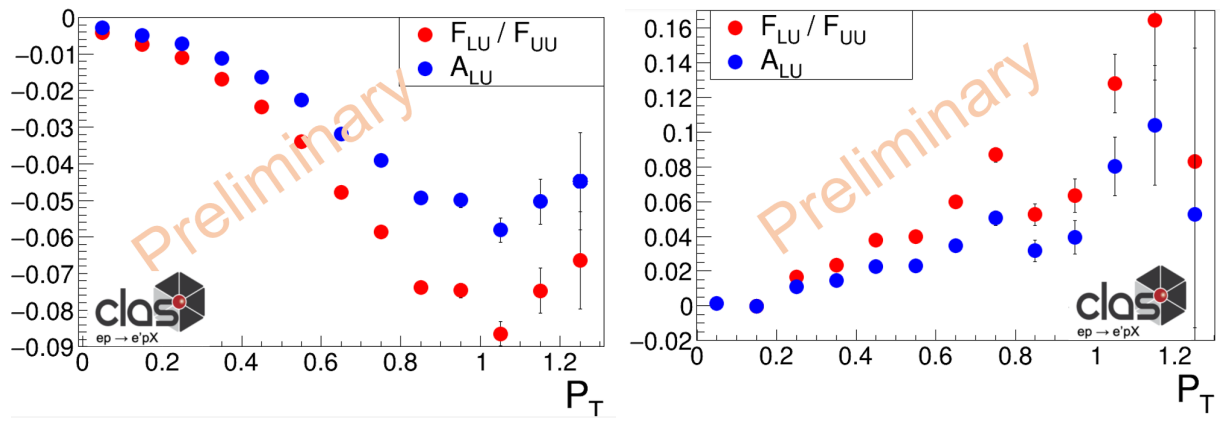


Figure 38: SSAs and ratios of Fracture Functions for the Proton Transverse momentum in the TFR (Left) and the CFR (Right).

372 **References**

- 373 [1] L. Trentadue and G. Veneziano, “Fracture functions: An Improved description of inclusive hard
374 processes in QCD,” *Phys. Lett.*, vol. B323, pp. 201–211, 1994.
- 375 [2] M. Anselmino, V. Barone, and A. Kotzinian, “SIDIS in the target fragmentation region: polarized
376 and transverse momentum dependent fracture functions,” *Phys. Lett.*, vol. B699, pp. 108–118,
377 2011.
- 378 [3] A. Kotzinian, “New quark distributions and semiinclusive electroproduction on the polarized
379 nucleons,” *Nucl. Phys.*, vol. B441, pp. 234–248, 1995.
- 380 [4] P. J. Mulders and R. D. Tangerman, “The complete tree-level result up to order 1/q for polarized
381 deep-inelastic lepto production,” *Nucl. Phys.*, vol. B461, pp. 197–237, 1996.
- 382 [5] A. Bacchetta *et al.*, “Semi-inclusive deep inelastic scattering at small transverse momentum,”
383 *JHEP*, vol. 02, p. 093, 2007.
- 384 [6] e. a. Bacchetta, “Semi-inclusive deep inelastic scattering at small transverse momentum ,” *JHEP*,
385 vol. 02, p. 093, 2001.
- 386 [7] H. Avakian *et al.*, “Measurement of beam-spin asymmetries for deep inelastic pi+ electroproduction,”
387 *Phys. Rev.*, vol. D69, p. 112004, 2004.
- 388 [8] S. Diehl *et al.*, “First multidimensional, high precision measurements of semi-inclusive π^+ beam
389 single spin asymmetries from the proton over a wide range of kinematics,” 1 2021.
- 390 [9] T. B. Hayward, C. Dilks, A. Vossen, H. Avakian, *et al.*, “Observation of beam spin asymmetries
391 in the process $ep \rightarrow e' \pi^+ \pi^- x$ with CLAS12,” *Phys. Rev. Lett.*, vol. 126, p. 152501, Apr 2021.
- 392 [10] A. Airapetian *et al.*, “Beam-spin asymmetries in the azimuthal distribution of pion electropro-
393 duction,” *Phys. Lett.*, vol. B648, pp. 164–170, 2007.
- 394 [11] T. B. Hayward, “Dihadron beam spin asymmetries on an unpolarized hydrogen target with
395 CLAS12.” Thesis, College of William & Mary, available at https://www.jlab.org/Hall-B/general/thesis/THayward_thesis.pdf, 2021.
- 396 [12] S. Diehl and K. Joo, “A multidimensional study of sidis π^+ beam spin asymmetry over a wide
397 range of kinematics..” Internal Note., 2020.
- 398 [13] CLAS, “11 GeV polarized electrons on liquid hydrogen target to study proton structure, 3d
399 imaging, and gluonic excitations, RG-A analysis overview and procedure.” Internal Note, under
400 review. Snapshot from August 2020: https://clas12-docdb.jlab.org/DocDB/0009/000949/001/RGA_Analysis_Overview_and_Procedures-08172020.pdf.
- 401 [14] A. Kim, S. Diehl, and K. Joo, “Analysis note on deeply virtual π^0 electroproduction with
402 CLAS12.” Internal CLAS analysis note, available at https://clas12-docdb.jlab.org/DocDB/0009/000948/001/AKim_pi0_note.pdf, 2021.
- 403
- 404
- 405